Effect of loading direction on the critical characteristic strength and energy evolution of quartz mica schist and microscale mechanisms

Xiaomeng Yin[1,2] · Xia Zhang[2] · Yuju Lei[3] · Lunan Wang[4]

Abstract

In this study, micro and uniaxial compression tests were performed on two types of quartz mica schist. The effect of schistosity orientation on their mechanical properties was discussed in terms of the critical characteristic strength (CCS) and energy. Furthermore, the microscale mechanism of the mechanical properties of schistose rocks was revealed. In view of the good correspondence between the energy evolution curves and stages of rock damage, the damage evolution process of rock before failure can be divided into five stages. Energy evolution curves can be used to quickly and accurately determine the CCS of specimens, including the initiation, closure, and damage strength of cracks. This suggests that the energy and CCS of schist depend closely on the schistose angle α. The specimen with $\alpha = 30°$ has the minimum crack initiation strength and the highest level of crack initiation stress, while the specimen with $\alpha = 90°$ has the lowest level of crack damage stress and higher elastic and dissipation energy. The mechanical anisotropy, closely related to the orientation dependence of crack initiation and propagation, is essentially controlled by the typical interbedded quasi-microstructure composed of clustered mica layers and granular mineral layers. The CCS and energy are significantly different for the two tested schist samples, and they are determined by microscale factors, such as the proportions of soft and hard minerals, aggregation degree of flaky minerals, and continuity of oriented mica clusters. The CCS and energy of schistose rocks are more sensitive to the various microscale factors at $\alpha = 30°$ than at $\alpha = 90°$.

Keywords Schistose rock · Anisotropy · Critical characteristic strength · Energy · Microscale mechanism

Introduction

The mechanical properties of many metamorphic and sedimentary rocks and a few igneous rocks change with the loading direction due to the characteristics of inherent weak planes, such as texture, bedding, schistosity, and foliation. As a common property of heterogeneous rock, anisotropy has long attracted the attention of rock mechanics researchers and geotechnical engineering experts. Anisotropy is often considered an important factor in the stability analysis and support design of various rock engineering projects, and ignoring anisotropy can produce erroneous results of differing magnitudes (Kim et al. 2012). Especially in underground engineering projects, asymmetric deformation and local fracture of the structure and bolt failure are likely to occur because of the anisotropy of the surrounding rocks. Focusing on fundamental mechanical properties involving the strength and deformation of anisotropic rocks, many researchers have performed fruitful research on the response laws of mechanical indexes such as peak strength, elastic modulus, and Poisson's ratio to the loading direction (Donath 1964; Hoek 1964; Nasseri et al. 2003; Cho et al. 2012; Gholami and Rasouli 2014), and the macroscopic mode of failure of anisotropic rocks (Mclamore and Grey 1967, Ramamurthy et al. 1993, Niandou et al. 1997, Tien et al. 2006, Khanlari et al. 2015). For the convenience of

✉ Yuju Lei
leiyuju0903@163.com

1 College of Intelligent Construction, Wuchang University of Technology, Wuhan 430223, China

2 College of Architecture and Civil Engineering, Xinyang Normal University, Xinyang 464000, China

3 School of Education, Hubei University of Art and Science, Xiangyang 441053, China

4 School of Civil Engineering, Liaoning Petrochemical University, Fushun 113001, China

engineering applications, great efforts have been made to develop a series of empirical or theoretical formulas for the prediction of mechanical indexes (Walsh and Brace 1964; Bieniawski 1974; Rao et al. 1986; Duveau et al. 1998; Saroglou and Tsiambaos 2008).

Many rocks subjected to compression loading display brittle failure characteristics. With increasing compressive stress, the original cracks in brittle rocks are compressed and closed, new cracks are initiated and expanded, and finally, multiple cracks coalesce to form a fracture plane. Consequently, rock failure is accompanied by a great reduction or loss of loadbearing capacity. Based on the characteristics of crack evolution and changes in rock structure, the deformation and failure of rocks under compression has been divided into different stages. Accordingly, several characteristic strengths are used as important critical indexes to describe the mechanical properties of brittle rocks. A thorough understanding of crack development and the critical characteristic strength of brittle rocks is of great significance for analyzing the failure mode of rocks, ensuring the effectiveness of support and evaluating the long-term stability of geotechnical engineering projects. Especially for deep tunneling in brittle rock, a slabbing failure of the wall rock subjected to the equivalent uniaxial stress often arises before the principal stress reaches the laboratory peak value. This interesting phenomenon, caused by the difference of stress environment between in situ and laboratory, essentially involves crack evolution characteristics of brittle rocks. Diederichs et al. (2004) proposed that the lower and upper bounds for in situ strength of the brittle rock near the excavation face correspond to the stress thresholds of crack initiation and coalescence from lab tests, respectively. In this regard, it is limiting to pay attention only to the fundamental mechanical performance of rock at the peak loading point.

The essence of brittle failure of rocks involves the gradual evolution of crack systems accompanied by structural damage and energy transformation. It is gradually realized that the complex strength change and overall failure behavior of rock could be nicely described from the energy point of view. In recent years, the principle of energy dissipation and release has been widely considered in the field of rock mechanics and engineering and this principle has been applied to the identification of rock instability (Griffith 1921; BАńKa et al. 2017), brittleness evaluation (Zhang et al. 2017; Chen et al. 2020), and rockburst prediction (Kidybinski 1981; Cai et al. 2001; Yang et al. 2019). However, most of the previous studies focused on isotropic rocks. There is much need for relevant advances related to rocks with weak planes.

In addition, long-distance tunnel engineering projects passing through mountainous areas where there are distributions of regional metamorphic rocks, typical representatives of anisotropic rocks, often face with complex lithological changes due to different formation environments and protolith distributions. Even rocks with the same mineral composition may exhibit significantly different degrees of mechanical anisotropy. Taking Tongsheng Tunnel located in Shiyan City, Hubei Province, China, as an example, the rock surrounding is mainly composed of light gray-white Wudang group schist containing quartz and mica minerals. The degree of schistosity development along the tunnel axis varies greatly with spatial location, resulting in inconsistent mechanical anisotropy behavior. After summarizing the test results of some researchers (Wang et al. 2014; Li 2017; Xu 2018; Yin et al. 2020), the anisotropy degree of this set of schist was found to vary widely, even up to two to three times the difference. If the same set of parameters are used without differentiation for the general support of schistose rocks surrounding projects, additional expenses or disastrous consequences will be produced due to excessive or insufficient support. It may be a reasonable decision to divide the surrounding rocks into different zones for targeted support according to their significant mechanical properties. The macromechanical properties of rocks are essentially controlled by their fabric. The anisotropy degree of heterogeneous rocks with the same composition must be affected by the mineral content and microstructure. Investigating the mechanism for microscale effects on macromechanical properties and response laws of anisotropic behavior is not only helpful for the implementation of reasonable engineering support but also conducive to the in-depth understanding of the failure mode of anisotropic rocks, which will provide a sound theoretical basis for the establishment of more reliable mechanical criteria.

In this study, two types of quartz mica schist with different appearance characteristics were selected. Micro tests were performed on the rock samples by polarizing microscopy and environmental scanning electron microscopy to mainly analyze the mineral composition and microstructure and summarize the differences in microscale factors between the two types of schist. Then, cylindrical schist specimens with representative schistose angles were prepared to investigate their mechanical properties by uniaxial compression testing. The main purposes of the present study are as follows:

(1) To analyze the effect of schistosity orientation on the critical characteristic strength and energy evolution of compressed schist during deformation, damage, and failure.
(2) To reveal the microscale mechanism affecting macroscale mechanical properties of schistose rocks and discuss the laws for the response of the anisotropic behavior of schist to microscale factors.
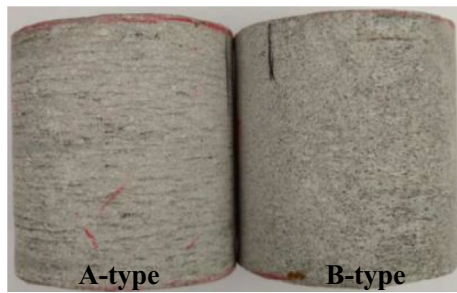
Fig. 1 Schist samples

Physical properties and fabric of samples

Physical properties

Two schist samples with different appearance characteristics, labelled A-type and B-type, were taken from the Tongsheng Tunnel. There are obvious schistosity planes in A-type schist and faintly visible planes in B-type schist (Fig. 1). Compared with B-type schist, A-type schist has a less crisp sound when hammered, and its end surfaces exhibit a significantly stronger silky luster due to the presence of considerable amounts of mica minerals. The results of physical tests show that the dry density and saturated density of A-type schist are 2.662 g/cm^3 and 2.684 g/cm^3, respectively. Correspondingly, the dry and saturated densities are 2.675 g/cm^3 and 2.688 g/cm^3 for B-type schist. The P-wave test reveals that the wave velocities in the two types of schist vary as a function of the direction of wave propagation, showing different degrees of orientation dependence. The P-wave propagating parallel or perpendicular to schistosity planes have the maximum or minimum velocity, respectively. Overall, the P-wave velocity of A-type schist varies from 2785 m/s to 5351 m/s, with an anisotropy degree of 1.92, while the velocity of B-type schist varies in the range from 3719 m/s to 5042 m/s, with an anisotropy degree of 1.36.

Mineral composition and microstructure

To analyze the mineral composition and observe the typical microstructure of schist as comprehensively as possible, two types of rock samples were cut along the direction perpendicular to the schistosity planes, and thin sections and optical sections were obtained through a series of procedures. Then, polarizing microscopy (PLM) and environmental scanning electron microscopy (ESEM) were used to carry out micro tests, relying on the advantages of the reliability of qualitative analysis on mineral composition and the high precision of microstructure observation.

PLM reveals that the two types of schist have the same mineral composition and are mainly composed of quartz, mica, feldspar, and calcite (Fig. 2). Therefore, the tested samples should be classified as quartz mica schist in terms of mineralogy. According to their morphological characteristics, the minerals can be divided into two types. One type is granular minerals, mainly including quartz, feldspar, and calcite. The other type is flaky minerals, represented by mica and a small amount of chlorite, a weathering product of mica. As a typical feature of regional metamorphic rocks, both types of minerals show a certain degree of unidirectional elongation. The preferred orientation of flaky mica is particularly developed and plays a major role in the anisotropy of rocks. As shown in Fig. 2, flaky mica tends to aggregate into clusters, and multiple mica clusters are distributed discontinuously in the same layer. Adjacent mica clusters are filled with granular minerals to form hard mineral zones. Mica clusters and hard mineral zones are distributed alternately, making up a weak layer. In the direction perpendicular to the extension of weak layers, there is an interbedded quasi-structure consisting of weak layers mainly containing flaky minerals and hard layers composed of granular minerals.

Fig. 2 Mineral composition and distribution of schist samples. (**a**) A-type schist. (**b**) B-type schist

(**a**) A-type schist   (**b**) B-type schist
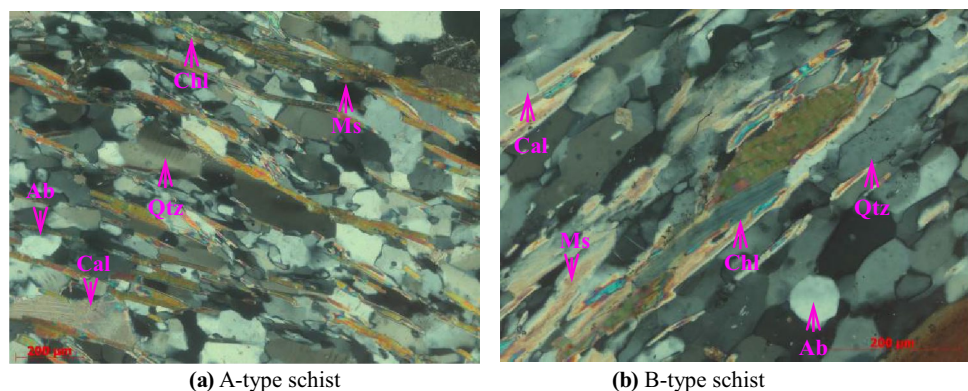
In comparison, the two types of schist are obviously different in the relative proportions of flaky and granular minerals, degree of mica aggregation and continuity of oriented mica clusters in the same layer. With the aid of ESEM, these differences can be further revealed quantitatively. First, grayscale images were acquired by ESEM. Analysis of the chemical composition at the designated points was then carried out. Combined with the results of mineral composition analysis by PLM, the mineral corresponding to each gray value was determined. Next, the digital image processing software ImagePro Plus (IPP) was utilized to divide various minerals according to brightness (Fig. 3 shows the division results) and count the areas of the mineral particles. The proportion of particle areas of each major mineral in the total image area was obtained.

The results show that in the A-type and B-type schist, flaky mica minerals account for 17.2% and 11.6%, respectively, and granular minerals containing quartz, feldspar, and calcite account for 82.7% and 88.2%, respectively. The long axis of the mica cluster was also measured and counted by IPP. The average length is approximately 360 μm and 110 μm for A-type and B-type schist, respectively. The length of the hard mineral zone between the adjacent oriented mica clusters has been roughly counted, and the value is mainly in the range of 50–200 μm for A-type schist and 250–350 μm for B-type schist. Thus, A-type schist has a smaller proportion of hard granular minerals, a higher degree of mica aggregation, and a better continuity of oriented mica clusters in the same layer than B-type schist. As a result, flaky minerals in A-type schist overall have a more regularly oriented distribution of layers, while the distribution of flaky minerals in B-type schist is slightly more disordered than those in A-type schist.

The defects containing pores and microcracks in the rock samples are also clearly observed by ESEM (Fig. 4). The pores are randomly distributed at the contact points
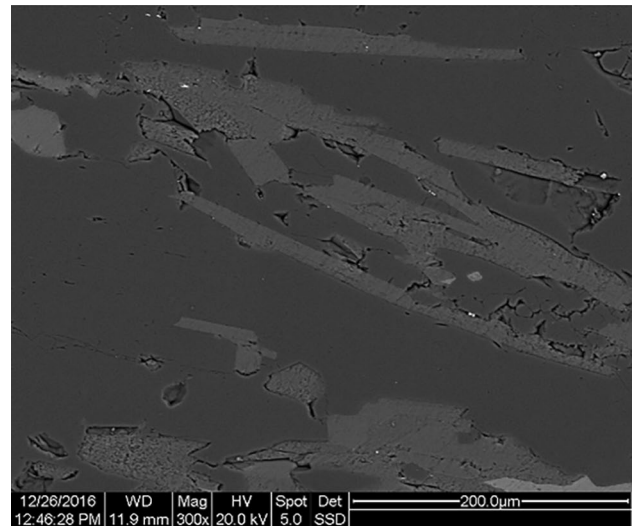

Fig. 4 Grayscale image obtained by ESEM

of granular minerals, while the microcracks have a certain degree of orientation due to their strong spatial dependence on the mica clusters. Microcracks tend to be distributed at the edges of mica clusters due to mechanical weakness at this location. In contrast, large microcracks are less developed in B-type schist, which consequently has a denser structure than A-type schist.

Mechanical testing and analysis

Specimen preparation

The maximum compressive strength of schistose rocks appears at $\alpha = 0°$ or $90°$ (α represents the angle between the loading direction and schistosity planes), while the minimum

Fig. 3 Division of minerals by Imagepro plus (IPP) (quartz and feldspar; mica; calcite; chlorite; pyrite). (**a**) A-type schist. (**b**) B-type schist
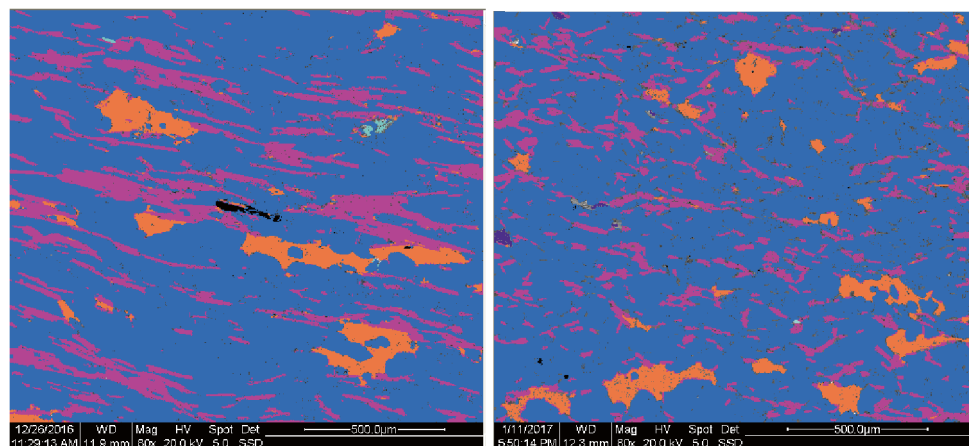
(a) A-type schist

(b) B-type schist

value appears in the range of $\alpha = 20°–50°$ (Mclamore and Gray 1967; Ramamurthy et al. 1993; Niandou et al. 1997; Nasseri et al. 2003; Khanlari et al. 2015) and was determined to be $\alpha = 30°$ for the target schist samples in our previous study (Yin 2017). In the present work, the two types of schist were made into cylindrical specimens (100 mm in height and 50 mm in diameter) with three representative schistose angles of 0°, 30°, and 90°. Then, the prepared specimens were oven-dried at 105 °C for 24 h. P-wave measurements were performed on the dried specimens to conduct further screening. Finally, a group of specimens with $\alpha = 0°$, 30°, and 90° were obtained for each type of schist for uniaxial compression testing. Four extensometers were symmetrically arranged at the mid-height of the specimens to monitor lateral strain during the test.

Stress–strain curves

The stress–strain curves present obvious strain-softening characteristics, indicating the brittleness of schist samples (Fig. 5). All specimens go through the stages of compaction, linear elastic deformation, and elastoplastic deformation before failure. The curves of specimens with various schistose angles reveal the significant anisotropy of quartz mica schist in terms of the mechanical behavior, which involves the following performance:

(a) During early loading, there is better axial compaction for $\alpha = 90°$, which is attributed to the more intense compressed closure of defects dominated by oriented microcracks after the specimen was subjected to perpendicular axial stress. In contrast, relatively inconspicuous compaction exists in the specimen with $\alpha = 0°$, suggesting the insensitive response of the initial axial deformation

to the axial stress due to the main contribution of small-sized intergranular pores to compression deformation in the case where there are large microcracks parallel to the axial stress.

(b) For the curve of the specimen with $\alpha = 0°$, the maximum slope is in the linear elastic section and the minimum value is at $\alpha = 90°$, which is closely associated with the main controlling unit layer resistant to elastic deformation inside the schist characterized by a interbedded quasi-structure. At $\alpha = 0°$, the soft layer containing flaky minerals and the hard layer composed of granular minerals are compressed parallel to the axial load. The compression deformation of the specimen is mainly borne by the rigid layer, consequently causing a larger elastic modulus. At $\alpha = 90°$, the soft and hard layers are compressed perpendicular to the axial load. The soft layer with slight stiffness makes a dominant contribution to the compression deformation of the specimen, and the elastic modulus is relatively small as a result.

(c) The specimen with $\alpha = 90°$ exhibits a more distinct elastoplastic deformation stage, and a more obvious yield occurs when the load is close to the peak value. The yield involves the crack propagation characteristics of schistose specimens, which will be discussed in detail below.

(d) At the peak point, the specimen with $\alpha = 0°$ has the maximum lateral strain, while the specimen with $\alpha = 90°$ has the maximum axial strain, suggesting the close dependence of the Poisson effect on the loading direction for schistose rocks.

Evolution stage of compressed specimen

The failure of brittle rocks is essentially caused by the initiation and propagation of cracks. In this regard, brittle rocks
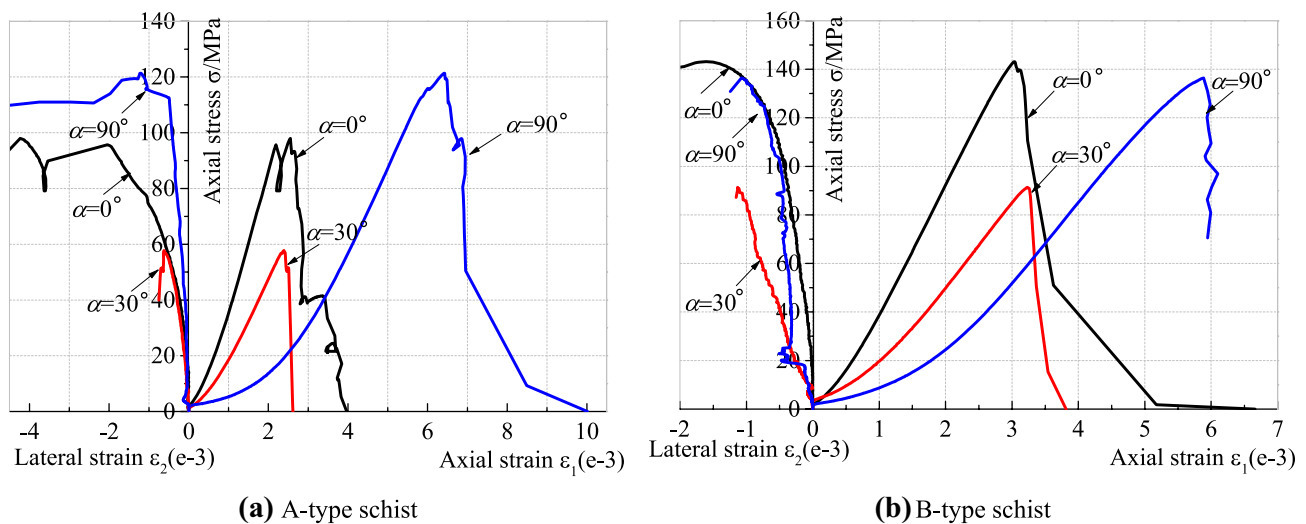
Fig. 5 Stress–strain curves of schist specimens. (**a**) A-type schist. (**b**) B-type schist

subjected to compression loading undergo several stages involving compaction, linear elasticity, stable crack growth, and accelerated crack growth. At the initial stage of loading, rock is compacted with a decrease in the defect rate due to compression and closure of open internal pores and microcracks. After reaching the crack closure stress, the compacted rock undergoes reversible elastic deformation similar to an elastic material. Then, new cracks are initiated by stress concentrations at a certain critical stress, indicating the onset of crack growth. In the early stage of crack growth (stable crack growth stage), crack propagation occurs only when the stress increases continuously, implying the stable and independent growth of cracks. The crack growth rate increases once the cracks begin to coalesce, which represents the advent of an accelerated growth stage, characterized by the continuous growth of cracks even if the stress remains constant. At this stage, the rapid increase in crack density causes the most significant change in the structure of rock, and the volumetric strain of rock changes from the previously dominant compression to overwhelming expansion. Finally, the unsteady developing cracks interconnect to form a macroscopic fracture plane, which leads to rapid attenuation or even loss of rock strength.

Several significant axial stress thresholds are involved in the evolution of deformation and failure of brittle rocks, that is, the crack closure stress (σ_{cc}) at the beginning of the elastic stage; the crack initiation stress (σ_{ci}) at the end of the elastic stage; the crack damage stress (σ_{cd}) representing the transition from stable crack growth to accelerated crack growth; and the peak stress (σ_f) at rock failure. These stress thresholds correspond to several important critical characteristic strength (CCS) values of brittle rocks under compression. The accurate determination of the CCS of brittle rocks is of great practical significance for the establishment of strength criteria and the stability evaluation of surrounding rocks for deeply buried tunnels.

The methods for determining the CCS mainly include the acoustic emission measurement method and strain measurement method (Bieniawski 1967; Martin and Chandler 1994; Eberhardt et al. 1998, 1999). Affected by parameter settings, noise, etc., acoustic emissions have not been widely applicable for the determination of the CCS (Zhou et al. 2015). The commonly used strain measurement methods include the volume strain method, moving point regression method, crack volume strain method, etc. Here, based on the moving point regression method, the change in axial strain stiffness of specimens subjected to continuous compression was obtained to first determine the crack closure strength (σ_{cc}) and crack initiation strength (σ_{ci}) of schist. Considering the human error of this traditional method, we have proposed a simple method to improve the accuracy of the results (Yin et al. 2020). As shown in Fig. 6 (taking the B-type specimen with $\alpha = 90°$ as an example), the axial stiffness (represented
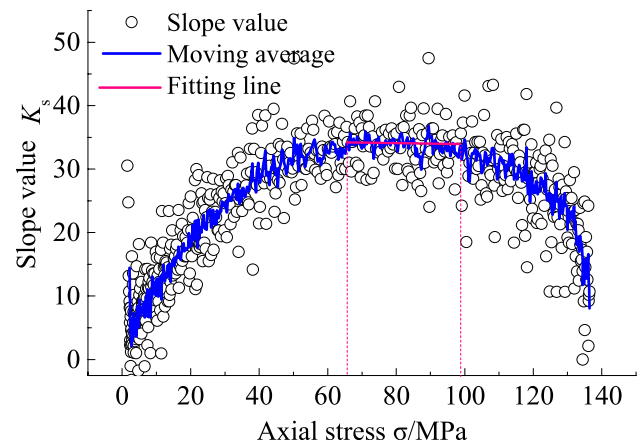

Fig. 6 Determination of axial stress range in linear elastic stage

by hollow circles in Fig. 6) was calculated using the axial stress and strain data of adjacent monitoring points. The moving average regression method was then utilized to obtain a stiffness curve that clearly followed a variation law. By multiple fits of the axial stiffness data corresponding to the near-horizontal section of the curve, the best linear elastic stage was determined, represented by the near-horizontal line in Fig. 6. The axial stress indicated by the two ends of the line corresponds to σ_{cc} and σ_{ci}. As the stress turning point of volume compression to volume expansion, the crack damage stress (σ_{cd}) can be easily determined by the volume strain method. A scatter plot of the volumetric strain–axial strain was drawn, as shown in Fig. 7 (taking the B-type specimen with $\alpha = 90°$ as an example). The peak point of the volumetric strain corresponds to the crack damage point. Combining the axial stress–strain curve, the axial stiffness curve, and the volumetric strain curve, the CCS of schist specimens subjected to axial compression can be quickly determined
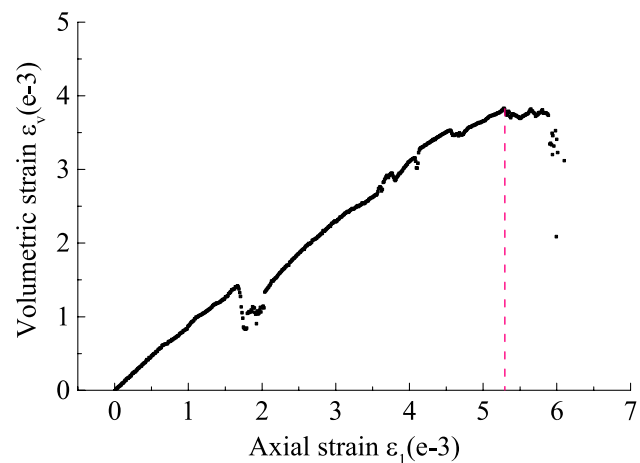

Fig. 7 Determination of crack damage point based on volume strain method

Table 1 Critical characteristic strength of schist specimens determined by strain measurement method

Critical characteristic strength	Specimens no. and strength values (MPa)					
	A0	A30	A90	B0	B30	B90
σ_{cc}	47.83	31.13	61.43	54.11	51.85	66.90
σ_{ci}	68.05	44.23	90.32	109.47	73.64	96.89
σ_{cd}	52.26*	53.78	111.38	104.33*	85.78	123.05
σ_{f}	97.96	57.80	121.37	143.11	91.37	136.41

The letter of specimens no. represents the type of rock sample, and the number represents the schistose angle.“*”indicates value abnormity

(Fig. 8). The results are shown in Table 1. Unlike $\alpha = 30°$ and $\alpha = 90°$, σ_{cd} is smaller than σ_{ci} at $\alpha = 0°$ for both types of schist. This result is obviously counterintuitive, which may be attributed to the fact that when the compression load is applied parallel to schistosity planes, there is a relatively large lateral strain before new cracks appear in the specimen.

Analysis of energy evolution and critical characteristic strength

Based on the energy damage and fracture mechanism, the deformation and failure of rocks under compression involves a series of complex energy evolution processes, including energy input, accumulation of released elastic strain energy, energy dissipation, and energy release at the time of rock failure. Assuming that there is no heat exchange during the loading and unloading of rocks, the energy only exists in the form of elastic energy and dissipation energy in consideration of energy conservation. In the stress–strain curve, the work done by a testing machine on the specimen, that is, the total input energy, can be expressed as the area enclosed by the loading curve and strain axis (Fig. 9). One part of the total energy will be stored as elastic energy inside the rock and can be released by machine unloading. The instantaneous release of high elastic energy is believed to internally trigger the sudden destruction of brittle rocks (Xie et al. 2005). The area enclosed by the unloading curve and strain axis represents the releasable elastic energy (Fig. 9). The other part of the total energy is dissipated during the loading process, causing irreversible deformation of rocks. In addition to small amounts of heat, sound, and electric radiation energies, more dissipation energy is used for the damage and plastic deformation of rock, which are inseparable from the evolution of internal cracks in brittle rock. In the evolution process, the energy absorbed by rock is mainly converted into the surface energy of new cracks, plastic potential energy in the vicinity of the crack tip and heat energy produced by the friction of rock material. Therefore, energy dissipation is always accompanied by rock deformation and damage, expressed as the area enclosed by the loading curve, unloading curve and strain axis (Fig. 9). Thus, the total energy U, elastic energy U^e, and dissipation energy U^d of rocks in the process of deformation and failure follow the expression:

$$U = U^e + U^d \tag{1}$$

For the case of uniaxial compression, the total energy and elastic energy can be determined by curve integration.
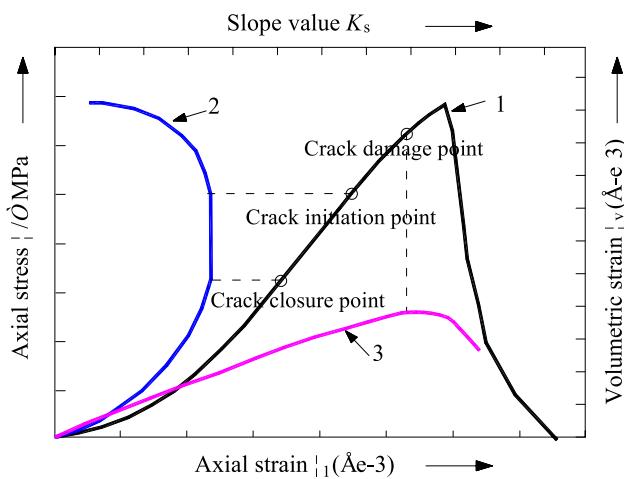
Fig. 8 Schematic diagram of determining critical stress points (curve 1: axial stress–strain curve; curve 2: Slope value–axial stress curve; curve 3: volumetric–axial strain curve. Arrows point to an increase in values)
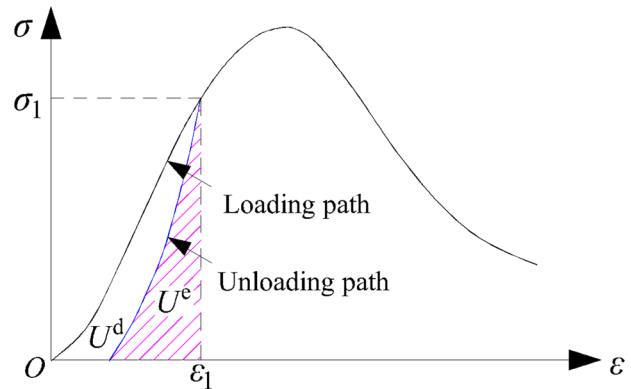
Fig. 9 Energy composition of rock during compression

$$U = \int \sigma_1 \mathrm{d}\varepsilon_1 \tag{2}$$

$$U^e = \frac{1}{2}\sigma_1 \varepsilon_1^e = \frac{1}{2E_u}\sigma_1^2 \tag{3}$$

where E_u is unloading elastic modulus.

The unloading elastic modulus fails to be obtained by a uniaxial loading test, which is often replaced by the loading elastic modulus E to carry out an approximate calculation. Then, the elastic energy of rocks subjected to continuous loading can be expressed as follows.

$$U^e = \frac{1}{2E}\sigma_1^2 \tag{4}$$

Therefore, the total energy, elastic energy, and dissipation energy of rocks can be calculated by formulas (1), (2), and (4).

The total, elastic, and dissipation energies before the peak loading point were plotted as a function of axial stress. As shown in Fig. 10, each type of energy–axial stress curve presents its inherent morphological characteristics. During the compression process, except for the irregular changes in energy due to inevitable slight unloading caused by local fracture (for example, the A-type specimen with $\alpha = 0°$), the total energy and elastic energy increase regularly as a power function of axial stress. According to the change pattern, the rising step-like dissipation energy–axial stress curve can be divided into three stages, characterized by a gradual decrease in slope (first stage), an approximate horizontal platform (second stage), and a rapid increase in slope, resembling an exponential function (third stage), respectively.

In the second stage, the dissipation energy remains unchanged due to the fact that the compacted rock acts as an elastic material to store all external work in the form of elastic energy. Therefore, this stage indicates the occurrence of linear elastic deformation of rock. The energy dissipation occurs in the first and third stages, namely compaction and elastoplastic deformation stages, accompanied by the closure of original defects and growth of new cracks, respectively. However, Fig. 10 reveals that the main stage of energy dissipation varies significantly with the loading direction. At $\alpha = 0°$ and $90°$, the energy is rapidly dissipated, and its quantity accounts for a quite high proportion of the total dissipation energy in the elastoplastic stage. At $\alpha = 30°$, the dissipation energy mainly increases greatly in the compaction stage; instead, the corresponding proportion is relatively low in the elastoplastic deformation stage.

The energy ratio, defined as the ratio of elastic energy to total energy, was utilized to quantitatively reveal the internal energy allocation law in different stages of deformation and failure. The curves of the energy ratio as a function of axial stress are shown in Fig. 10. They present an abnormally high energy ratio at the moment of initial instantaneous loading, followed by a brief sudden drop. If the initial energy change is ignored, the overall energy ratio gradually increases until a certain critical stress is reached, and then it tends to decrease instead. The turning stress point of the energy ratio curve nicely corresponds to the starting point of the sharp increase section in the third stage of the dissipation energy curve. In the elastoplastic deformation stage, once the independent cracks begin to coalesce and connect, the crack activity will become more intense, resulting in a significant increase in the energy dissipation rate. This means that accelerated crack growth can be represented by a sharp increase in dissipation energy, and the turning point of the energy ratio curve reasonably indicates the point of crack damage stress.

By virtue of the dissipation energy curve and energy ratio curve, the CCS of schist specimens subjected to uniaxial continuous loading can be accurately obtained, including σ_{cc}, σ_{ci}, and σ_{cd} (Fig. 10). The data shown in Table 2 were compared with those in Table 1 to find that their difference rate was only approximately 0.7–8.2% in terms of σ_{cc} and σ_{ci}. A small amount of basic data, including axial stress and strain, is enough to accurately determine the target values by the new method involving energy. In addition, this method can determine a reasonable σ_{cd} and compensate for the failure of the volume strain method in obtaining this critical characteristic strength of the schist specimen with $\alpha = 0°$. Therefore, the method for determining the CCS of schistose rocks by means of the energy evolution curves has definite advantages of convenience and accuracy. The energy curves of the two types of samples show a certain difference at $\alpha = 0°$. Except for the obvious irregular tortuosity in the curves of total energy and dissipation energy, the A-type schist has a shorter stress history during the sharp increase in dissipation energy than the B-type schist. This difference is relevant to microscale factors involving fabric in the two schist samples, which will be explained in detail below.

The final σ_{cc}, σ_{ci}, and σ_{cd} values comprehensively valued based on the strain measurement method and energy evolution curves are shown in Fig. 11, which presents the obvious schistosity orientation of the CCS. For both A-type and B-type schist, the variation in σ_{cc} with schistose angle follows $\alpha = 90° > \alpha = 0° > \alpha = 30°$. σ_{ci} and σ_{cd} show $\alpha = 90° > \alpha = 0° > \alpha = 30°$ for A-type schist, while $\alpha = 0° > \alpha = 90° > \alpha = 30°$ for B-type schist, which exhibits the same variation as the peak strength (Table 2). As an important mechanical index, peak strength (σ_f) is often considered in the design of supports for geotechnical engineering projects. However, it has been proved to be the instantaneous strength of rocks, which does not exist under long-term loading. Moreover, σ_f fails to represent the essential properties of rocks due to its correlation with external
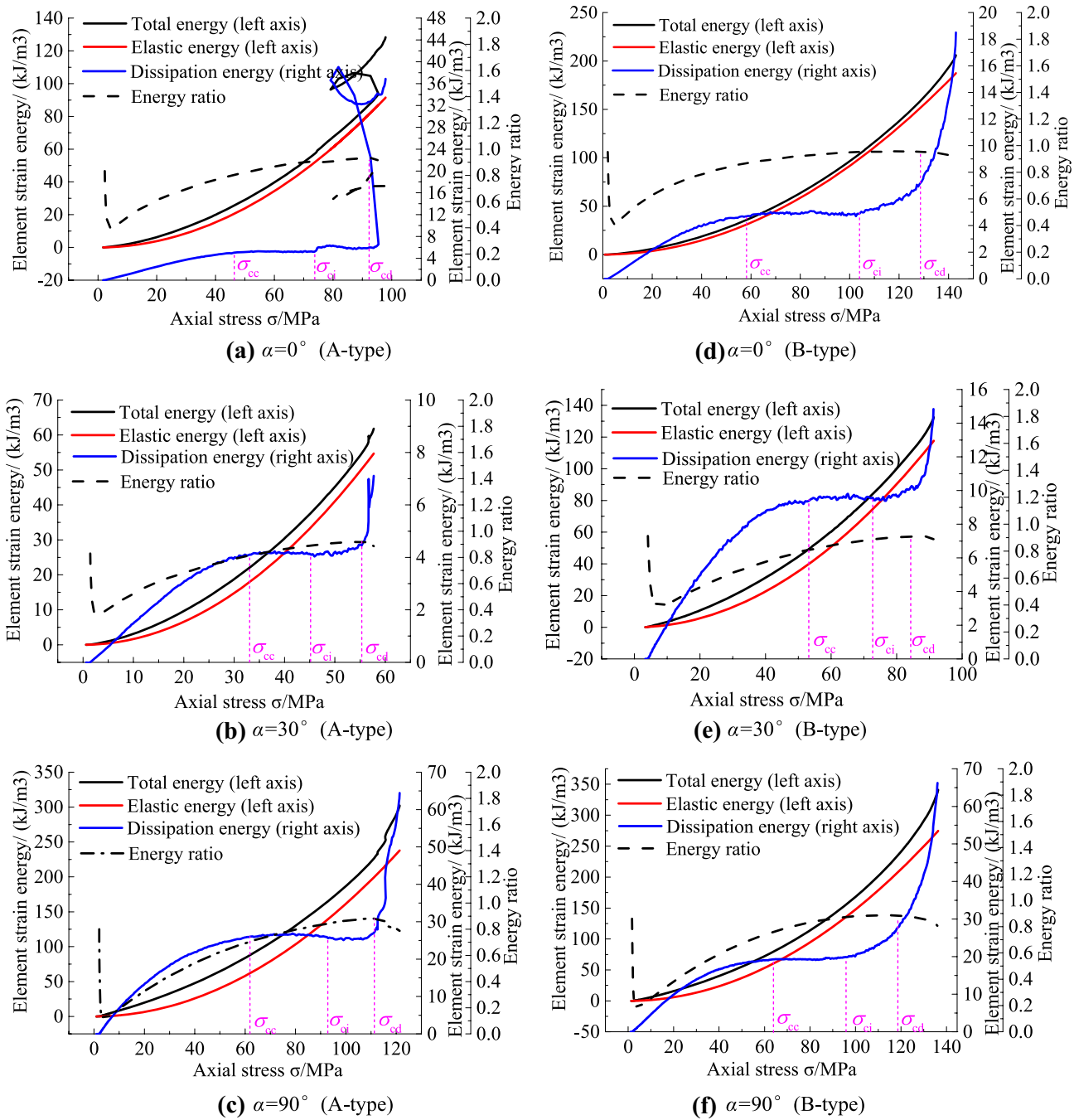
Fig. 10 Energy evolution curves of schist specimens (**a**) $\alpha=0°$(A-type). (**b**) $\alpha=30°$(A-type). (**c**) $\alpha=90°$(A-type). (**d**) $\alpha=0°$(B-type). (**e**) $\alpha=30°$(B-type). (**f**) $\alpha=90°$(B-type)

factors such as loading rate and specimen size. Free from the influence of these external factors, σ_{ci} and σ_{cd} have been regarded as indexes able to characterize the properties of rocks (Martin and Chandler 1994). In addition, σ_{ci} remains

Table 2 Critical characteristic strength of schist specimens determined by energy evolution curves

Critical characteristic strength	Specimens no. and strength values (MPa)					
	A0	A30	A90	B0	B30	B90
σ_{cc}	46.41	33.03	61.84	58.38	53.25	64.07
σ_{ci}	73.64	45.29	92.54	104.18	72.70	96.09
σ_{cd}	92.20	55.50	110.88	128.84	84.37	118.87
σ_{f}	97.96	57.80	121.37	143.11	91.37	136.41
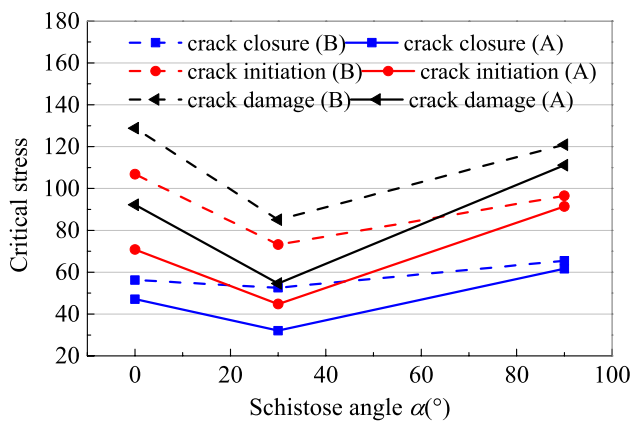
Fig. 11 Variation of critical characteristic strength of schist with the schistose angle

almost constant as the cycle times of loading and unloading increase, but σ_{cd} is closely related to the damage degree of rocks (Martin and Chandler 1994), which is inevitably influenced by the disturbance to the rock sample. In summary, it is more reliable to measure the degree of mechanical anisotropy of schistose rocks using the crack initiation strength σ_{ci} of specimens.

$R_{CI} = \sigma_{cimax} / \sigma_{cimin}$ (σ_{cimax} and σ_{cimin} are the maximum and minimum crack initiation strengths of the specimens with representative schistose angles) was used to evaluate the degree of mechanical anisotropy of the two types of schist. The results show $R_{CI} = 2.04$ and 1.46 for A-type and B-type schist, respectively. The CCSs of the two types of specimens with the same schistose angle were quantitatively compared using the ratio of the CCS for B-type and the CCS for A-type schists. The result, $\alpha = 30°$ (1.56–1.64) $> \alpha = 0°$ (1.19–1.51) $> \alpha = 90°$ (1.06–1.12), indicates that at $\alpha = 30°$, the CCSs of schistose rocks are more sensitive to its microfabric than at other angles. Therefore, for linear engineering projects located in the area of schistose rocks, close attention should be given to the parts in surrounding rocks where the maximum principal stress intersects with schistosity planes at an angle of 30°. On the one hand, the rocks in these parts

have lower strength. In addition, for rocks with the same lithology distributed in different spatial sections, there may be great strength differences in these parts due to diverse microscale factors. In this case, support design for the whole tunnel section that relies on the same empirical value may cause engineering-related accidents.

The energy value corresponding to each critical stress point was evaluated to explore the variation in energy with loading direction. As the data in Tables 3 and 4 show, the energy at $\alpha = 90°$ is higher than that at $\alpha = 0°$ and $\alpha = 30°$ for both schist samples. This suggests that the deformation and failure of schist require more external work, the rock has a greater energy storage limit, and more energy is dissipated for crack growth when the load is applied perpendicular to schistosity planes. The lower total and elastic energy at $\alpha = 30°$ than that at $\alpha = 0°$ indicates that the failure of schist requires less external work and the rock has less ability to store internal energy when the load is applied at an angle of 30° to the schistosity planes. The dissipation energy at $\alpha = 0°$ is like that at $\alpha = 30°$, except that the A-type specimen with $\alpha = 0°$ exhibits a significantly higher value than this type of specimen with $\alpha = 30°$ at the loading peak point, which may be related to its failure characteristics.

The change in energy with schistosity orientation can provide a good explanation for an interesting phenomenon in uniaxial compression testing; that is, flying rock fragments occasionally occur when the load is applied perpendicular to schistosity planes, while it infrequently occurs when the load is applied oblique to the planes. Accompanied by the failure of the specimen with $\alpha = 90°$ that has stored more elastic energy, a large amount of internal energy is released rapidly, part of which causes the rapid development of fracture planes, and part of which is converted into the kinetic energy of broken blocks.

In practical engineering projects, rockburst induced by tunnel excavation also involves the energy of rocks. The elastic energy index (W_{et}) is often used to predict the tendency for rockburst to occur, which can be determined exactly by loading and unloading tests. Under the stress path with only continuous loading, the elastic energy is approximated using the loading elastic modulus. In this case, W_{et} corresponds to the maximum ratio of the elastic energy to dissipation

Table 3 Energy values of A-type specimens at the critical stress points

Critical stress σ	Specimens no. and energy values (kJ/m³)								
	A0			A30			A90		
	U	U^e	U^d	U	U^e	U^d	U	U^e	U^d
σ_{cc}	26.49	21.40	5.09	21.07	16.96	4.11	87.40	61.36	26.04
σ_{ci}	53.43	48.25	5.17	36.93	32.81	4.12	161.09	135.05	26.05
σ_{cd}	87.24	81.28	5.97	53.64	49.16	4.48	227.40	200.17	27.23
σ_f	128.32	91.44	36.88	61.79	54.68	7.11	302.13	237.70	64.43

Table 4 Energy values of B-type specimens at the critical stress points

Critical stress σ	Specimens no. and energy values (kJ/m³)								
	B0			B30			B90		
	U	U^e	U^d	U	U^e	U^d	U	U^e	U^d
σ_{cc}	35.82	31.13	4.70	48.39	39.04	9.35	82.38	63.03	19.35
σ_{ci}	104.24	99.32	4.92	84.96	75.54	9.42	156.89	137.03	19.86
σ_{cd}	158.86	151.66	7.20	112.04	101.82	10.23	245.25	215.98	29.27
σ_{f}	205.93	187.42	18.51	132.45	117.61	14.84	340.81	274.58	66.23

energy in the process of energy evolution (Liu et al. 2020). The energy ratio curves in Fig. 10 show that the maximum ratio is located at the point of crack damage stress. Accordingly, the W_{et} of the tested specimens with $\alpha = 0°$, $\alpha = 30°$, and $\alpha = 90°$ are as follows: 13.6, 11.0, and 7.4 for A-type schist and 21.1, 10.0, and 7.4 for B-type schist, respectively. Thus, the surrounding rock at the position where the maximum principal stress is parallel to schistosity planes has a stronger tendency for rockburst to occur.

In addition, comparing the energy data for the two types of schist shows that the energy of B-type specimens is significantly higher than that of A-type specimens at $\alpha = 30°$, with a larger difference rate, while at $\alpha = 90°$, there is a smaller difference rate between the energies of the two types of schist.

The critical stress ratio R_{cs}, defined as the ratio of the critical stress to peak stress, was utilized to quantify the level of critical stress in each evolution stage. As shown in Fig. 12, overall, the levels of σ_{cc}, σ_{ci}, and σ_{cd} of the tested schist are in the ranges of 0.39–0.58, 0.72–0.80, and 0.89–0.95, respectively. Moreover, some common rules were revealed with respect to the effect of schistosity orientation for both two schist samples. (a) At $\alpha = 0°$, the schist has the minimum crack closure stress ratio, indicating that in this specific direction, the rock is compacted at a lower stress level due to the closure of the small-sized intergranular pores that mainly respond to the initial deformation. (b) The specimen with $\alpha = 30°$ has the maximum crack initiation stress ratio, suggesting that new cracks develop more rapidly and that the rock undergoes a shorter stress history from crack initiation to failure at $\alpha = 30°$. (c) The minimum crack damage stress ratio belongs to $\alpha = 90°$, suggesting that at $\alpha = 90°$, schist has a longer stress history corresponding to the accelerated growth stage, which is in good agreement with its better yield stage (Fig. 5). Furthermore, based on the comparison of the critical stress ratios of the two types of rocks, the lowest levels of σ_{cc} and σ_{cd} for A-type schist are higher than those for B-type schist, but the highest level of σ_{ci} is lower for A-type schist than B-type schist. This reveals that the B-type schist is more easily compacted at $\alpha = 0°$ and has a longer accelerated crack growth process at $\alpha = 90°$, while the A-type schist is more prone to initiate cracks at $\alpha = 30°$.
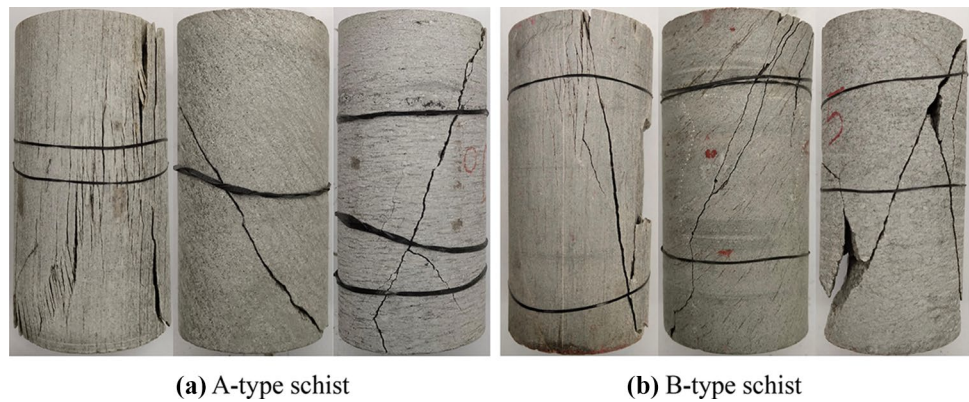
Discussion

Microscale mechanism for mechanical properties

Figure 13 shows the macroscopic failure patterns of schist specimens subjected to uniaxial compression. This suggests that the failure mode of schistose rocks closely depends on the loading direction. For both schist samples at $\alpha = 0°$, splitting failure occurs mainly along the schistosity planes; at $\alpha = 30°$, sliding failure occurs mainly along the schistosity planes; and at $\alpha = 90°$, the fracture plane obliquely intersects the schistosity planes. However, the two schist samples present some differences in the distribution characteristics and development degree of fracture planes. At $\alpha = 0°$, the fracture planes of the A-type sample are more developed and more densely distributed than those of the B-type sample. In addition, almost all the fracture planes extend along the schistosity planes. For the B-type sample, local fracture develops along the direction of oblique intersection with schistosity planes, which connects fracture planes distributed along different schistosity layers. At $\alpha = 30°$, a regular and flat fracture plane along the schistosity plane appears in
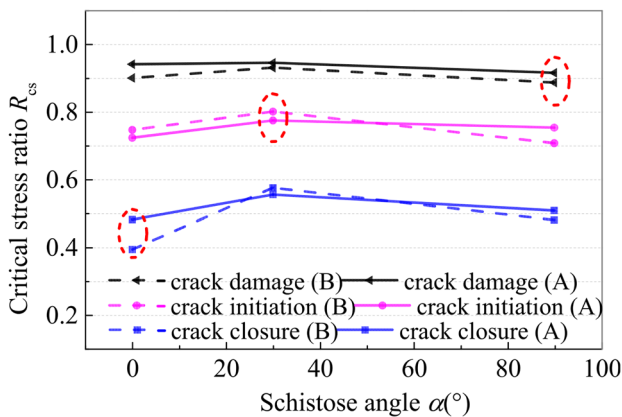
Fig. 12 Variation of critical stress ratio of schist with the schistose angle

(a) A-type schist   **(b)** B-type schist

the A-type sample, while in the B-type sample, the fracture plane deviates locally from the schistosity planes instead of fully following the path of the macroscopically weak planes. At $\alpha = 90°$, almost the same distribution of the main fracture plane is found in the two schist samples, but obviously, the secondary fracture planes are more developed in the B-type sample.

The strong brittleness of schist samples has been revealed by the stress–strain curves and rock failure patterns. The failure of brittle materials is characterized by gradual crack development and steadily increasing damage originating from the heterogeneity of materials. For compressed rocks, the microscale heterogeneity, caused by discrepant sizes and mechanical properties of mineral grains as well as pre-existing microcracks or pores, generally gives rise to the concentration of tensile stress. Owing to the poor resistance to tension compared to the shear capacity, new tensile cracks initiate at the stress concentration zone and propagate toward the direction of axial stress, which has been confirmed by compressibility tests (Matsushima 1960) and compressional wave velocity tests (Paulding 1965). Numerical simulations by discrete element code PFC revealed that tensile cracks dominate the failure process of the sample (Diederichs et al. 2004). However, it has been proven by experiments and theories that the growth of such tensile cracks is greatly influenced by the stress environment, and crack growth is easily arrested as cracks extend into the zones away from the initial crack point due to the confining stresses (Hoek and Bieniawski 1965). Especially in rock materials, the length of a tensile crack undergoing crack–boundary interactions is generally limited to the grain size at the initial stage of crack growth (Tapponier and Brace 1976). Therefore, isolated tensile cracks cannot lead to rock failure. Previous studies have shown that after the appearance of tension cracks, some secondary shear cracks occur at the ends of pre-existing flaws or between the initiated cracks (Bobet and Einstein 1998; Sagong and Bobet 2002). The overall failure of rock samples is often caused by the development of secondary cracks, which play an important role in the connection of cracks.

For anisotropic rocks, the orientation dependence of macroscopic failure is essentially controlled by microscopic characteristics. In the tested schist, the phyllosilicate minerals represented by flaky mica are prone to cluster into weak layers and tend to distribute in orientation. Hard layers composed of granular minerals and oriented weak layers are combined to form an interbedded quasi-microstructure. Additionally, the spatial distribution of the original microcracks in schist is restricted by that of mica clusters, which also show a certain degree of directionality. Previous studies indicate that phyllosilicate minerals play an important role in the crack evolution of brittle rocks. They can not only stimulate the formation of new cracks through intragranular sliding, kinking deformation, and incompatibility of crystal properties but also promote crack coalescence as a nucleus (Gottschalk et al. 1990; Chang and Haimson 2000; Federico et al. 2014). According to Griffith's theory, phyllosilicate minerals at the end of a slender crack are likely to produce stress several orders of magnitude higher than the far-field stress (Griffith 1921). Therefore, mica and microcracks in quartz mica schist are generally beneficial to crack development of rocks. When the loading angle α changes, the schist has various mechanisms of crack initiation and propagation, which further induce mechanical anisotropy with respect to the CCS and energy.

At $\alpha = 0°$, the weak and hard layers can be regarded as two kinds of upright bars with different stiffness values. Under vertical compressive stress, the difference in lateral strain between the two bars contributes to the concentration of tensile stress on their interface. On account of the low tensile strength at the edges of mica clusters, tensile cracks are apt to initiate at this location under compression and then propagate and coalesce in the hard mineral zones between adjacent mica clusters at the same layer level or in the hard layer between the weak layers, finally forming planes that undergo splitting on macroscopic scales mainly along the schistosity planes (Fig. 14a). In addition, crack initiation also easily occurs at the ends of oriented microcracks due to their low tensile strength. The above test data reveal low

Fig. 14 Crack propagation direction and distribution of fracture ▶ planes. (**a**) $\alpha = 0°$. (**b**) $\alpha = 30°$. (**c**) $\alpha = 90°$

dissipation energies due to the rapid growth of cracks along the schistosity plane.

At $\alpha = 30°$, wing cracks are readily initiated due to the concentration of tensile stress at the tips of mica clusters or microcracks caused by sliding along the cleavage plane of mica or microcrack surfaces under compression. The crack initiation mode of sliding under tension along these microscopically weak planes leads to a relatively small crack initiation stress. Initiated wing cracks grow parallel to the direction of the axial stress, and a release of the concentrated tensile stress occurs with the growth of cracks. Once the isolated wing crack propagates to its limit, a concentration of shear stress is formed again at the tip of microscopically weak planes, and quasi-coplanar secondary cracks initiate along the long axis of the planes (Bobet and Einstein 1998; Sagong and Bobet 2002). Then, the new shear cracks propagate and connect rapidly in the form of intergranular cracks in the hard mineral zone or the hard layer (Rawling et al. 2002) and finally form a macroscopic fracture plane that develops locally or wholly along the schistosity plane (Fig. 14b). This relatively inconspicuous stage of crack growth accounts for the higher level of crack initiation stress. The lower energy dissipation is mainly attributed to only a few intergranular and cleavage cracks during the damage evolution of rocks. A relatively flat macroscopic fracture surface, less crystal debris on the surface, and slight disturbance of minerals near the fracture path also provide proof to support this explanation.

Although both the specimens with $\alpha = 0°$ and $30°$ dissipate a small amount of energy during the processes of deformation and failure, they are still different in the main stages of energy dissipation. The above data reveal that at $\alpha = 0°$, the dissipation energy increases significantly in the crack growth stage, while at $\alpha = 30°$, more energy is dissipated in the compaction stage. As shown in Fig. 13, multiple fracture planes exist in the damaged specimen with $\alpha = 0°$. These macroscopic planes appear gradually along the schistosity planes of different layer levels. More energy is consumed for crack development, especially when cracks are on the verge of connectivity. At $\alpha = 30°$, the specimens only dissipate less energy in the stage of crack growth characterized by rapid propagation of a few cracks. Moreover, the difference in energy dissipation between $\alpha = 0°$ and $\alpha = 30°$ is more obvious in the A-type sample with more developed schistosity planes than in the B-type sample.

At $\alpha = 90°$, the concentrated stress is mainly produced at the ends of randomly distributed defects and on the interfaces between flaky and granular minerals, which triggers tension cracks in the hard zones or layers. New cracks gradually propagate and coalesce to form fracture planes

(**a**) $\alpha = 0°$

(**b**) $\alpha = 30°$

(**c**) $\alpha = 90°$
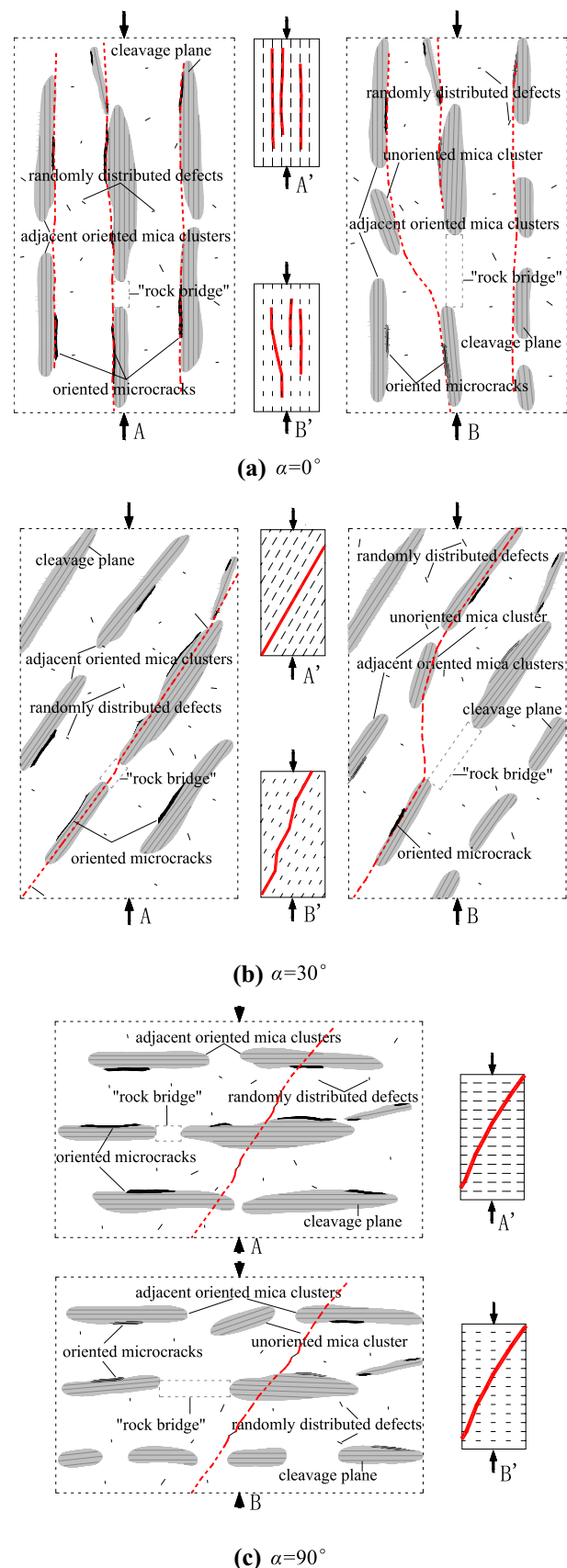
(Fig. 14c). Like isotropic rocks, the specimen with $\alpha = 90°$ has complex crack types, including transgranular cracks nearly parallel to compressive stress, intergranular cracks, and cleavage cracks with a large angle with respect to the compressive stress (Shea and Kronenberg 1993; Martin and Chandler 1994; Diederichs et al. 2004). The types of cracks are also found to be associated with the loading stage. Multiple intragranular cracks are first generated at a lower stress level, and these cracks continue to cut across the boundary of mineral particles to form transgranular cracks at a higher stress level (Martin and Chandler 1994). In view of the mechanical mechanism of cracks, the primary cracks, induced by concentrated tensile stress, generally occur prior to secondary cracks stemming from considerable shear stress. Although tensile cracks play a dominant role in the process of crack evolution, shear cracks are indispensable in the connection of cracks, eventually leading to the overall failure of rock. A pronounced increase in the number of shear cracks with the gradual evolution of the crack system has been revealed by analyzing the variation characteristics of acoustic emission parameters for gradually damaged brittle rocks, and such cracks are more likely to appear in the accelerated crack growth stage (Ohtsu et al. 2007; Wang et al. 2019).

Owing to the large number and various types of cracks, relatively wide fracture zones and irregular rough fracture planes are produced. Regarding energy, the specimen with $\alpha = 90°$ needs to store a large amount of elastic energy to drive the formation of different types of cracks, especially transgranular cracks, and the appearance of many cracks leads to a large amount of dissipation energy. In the yield stage, the cracks interact with each other strongly, and they will undergo a clearly demarcated gradation of coalescence and connection, leading to a lower level of crack damage stress at $\alpha = 90°$ than that at $\alpha = 0°$ and $30°$.

Some differences in the failure characteristics of the two schist samples indicate that for rocks with the same lithology, the crack propagation characteristics of specimens with specific schistose angles are closely associated with microscale factors, which mainly involve the spatial distribution and arrangement of mica in the tested schist. In the case of the large amount of aggregation of flaky mica, the good continuity of oriented mica clusters at the same layer level and the same short hard zone (regarded as a "rock bridge") filling adjacent oriented mica clusters, as shown in the A-type specimens with $\alpha = 0°$ and $30°$, the macroscopic fracture planes are almost always distributed along the schistosity planes (shown schematically by A' in Fig. 14 a and b). This is because the cracks extending into the short rock bridge connect rapidly prior to the coalescence of cracks forming in the hard layer (shown schematically by A Fig. 14 a and b). In the opposite case, as shown in the B-type specimens with $\alpha = 0°$ and $30°$, some macroscopic fracture planes present a

slightly stepped shape characterized by some parts developing at a small angle with the compressive stress and some parts developing along the weak layers (shown schematically by B' in Fig. 14 a and b). On the one hand, the long rock bridge fails to maintain the connection of cracks extended from the adjacent oriented mica clusters. Furthermore, mica minerals present a slightly disordered distribution in the opposite case, and the unoriented mica clusters often play a guiding role in the deviation of the crack propagation track from the extension direction of weak layers (shown schematically by B in Fig. 14 a and b). Crossed layers of cracks occur as a result. This phenomenon of crack propagation was confirmed by means of transmission electron microscopy in the study of (Shea and Kronenberg 1993).

The differences between the two schist samples in terms of the CCS and energy clearly manifest the influence of microscale factors on crack growth. Due to the good continuity of oriented mica clusters in A-type schist, cracks more easily propagate and coalesce, resulting in relatively flat fracture planes. Consequently, compared with B-type schist, A-type schist has obviously less dissipation energy at $\alpha = 30°$ (Tables 3 and 4) and a shorter stress history during the period of dissipation energy, increasing sharply at $\alpha = 0°$ (Fig. 10). However, the order of dissipation energy for the two samples at $\alpha = 0°$ is opposite to that at $\alpha = 30°$, which is related to the dense growth of multilayer cracks caused by the more developed weak layer in the A-type schist. In terms of the CCS, the more developed mica clusters and microcracks in A-type schist lead to its slower compaction at $\alpha = 0°$ and make it more likely to trigger crack initiation at $\alpha = 30°$. Therefore, in contrast to B-type schist, A-type schist presents a larger value at the lowest level of crack closure stress and a smaller value at the highest level of crack initiation stress.

At $\alpha = 90°$, the two rock samples present similar distributions of fracture planes, except that the secondary planes are more developed in the B-type schist, due to its stronger brittleness associated with less mica and more granular minerals, than in the A-type schist. Influenced by the proportions of soft and hard minerals, the CCS and energy data of the B-type specimen are expected to be overwhelmingly larger than those of the A-type specimen. However, in fact, the data show a small difference rate (Tables 2, 3, and 4), which is inseparable from the microstructure and schistosity orientation. Normally, flaky mica plays a beneficial role in the initiation and coalescence of cracks. However, when the extension direction of the mica cluster is perpendicular to the loading direction, it acts as a barrier to the cracks growing from the granular mineral layer and prevents their further propagation to a certain extent (Rawling et al. 2002). A higher driving energy needs to be stored to rupture the mica clusters for the connection of cracks in the adjacent granular mineral layers. With fewer granular mineral layers but more flaky mica layers, A-type schist, despite its relatively slight

amount of brittleness, has overall mechanical performance approximate to that of B-type schist. Additionally, considering that the mechanical properties of the A-type specimen are noticeably worse than those of the B-type specimen at $\alpha = 30°$, it is reasonable that the A-type schist has an obviously higher degree of anisotropy than the B-type schist. Therefore, for schists with the same mineral composition and controlled by typical microstructure, the mechanical anisotropy of compressed rocks is likely to present different salient degrees of performance as the microscale factors change.

Energy damage evolution of schistose rocks

From the microscopic perspective, the evolution of rock damage is a process of new crack initiation, propagation, and coalescence to form macroscopic fractures. Material destruction is an instability phenomenon driven by energy. Therefore, progressive damage of rock is always accompanied by energy evolution, which involves energy hardening and softening mechanisms (Chen et al. 2018). The energy hardening mechanism is manifested in the continuous accumulation of elastic energy in the process of rock deformation, which provides the energy source for ultimate rock failure. The energy softening mechanism is manifested in that the energy dissipation causes internal damage and crack propagation in rock, resulting in a decrease in its strength and energy storage capacity. The two mechanisms coexist during the entire deformation and failure process of rock. The energy hardening and softening mechanisms strengthen the ability to drive rock failure and reduce the ability to resist rock failure by gradual damage, respectively.

For the convenience of a unified analysis and to explore the universal laws of energy evolution during rock damage, the results of the elastic energy and dissipation energy during axial loading, divided by their respective total energy at the failure point, were plotted as normalized energy–axial strain curves. The energy ratio (ratio of elastic energy to total energy)–axial strain curve was used to analyze the rule of energy transformation in rock. Typical energy curves are shown in Fig. 15. Based on the characteristics of crack evolution and shapes of energy curves, the deformation and failure of brittle rocks subjected to uniaxial compression can be divided into the following five stages.

Stage I: instantaneous loading—initial stress distribution. When the external compressive load is suddenly applied to the end face of the rock, the stress cannot be transmitted to the interior of the rock in time, so original defects in the open state are not widely affected. The rock exhibits instantaneous elastic deformation, contributing to an abnormally high energy ratio. As the transfer of stress causes the initial distribution of internal stress in the rock, internal defects are compressed, accompanied by energy
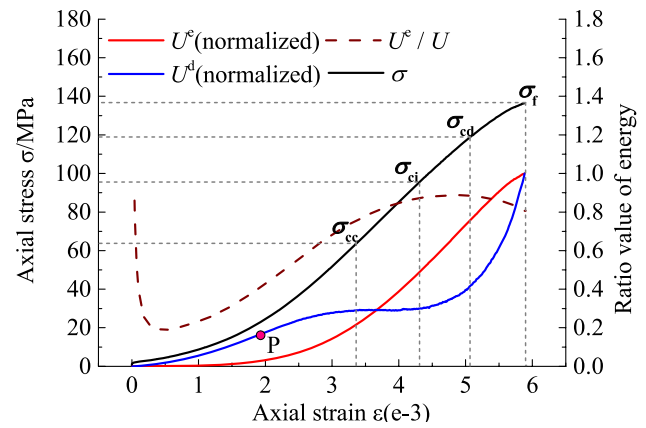
Fig. 15 Division of evolution stages of brittle rock under compression based on energy curves

dissipation, which leads to a rapid decrease in the energy ratio in the initial stage of loading.

Stage II: compaction—initial energy dissipation. Internal defects in rocks such as pores and microcracks are constantly undergoing compression and closing, resulting in the gradual compaction of the rock and an increase in stiffness. As the strain increases, the rate of elastic energy accumulation gradually increases, and the energy ratio continually increases. Due to the closure of defects, irreversible plastic deformation of rock occurs, accompanied by a small amount of energy dissipation. During the compaction of rock, the most open and largest defects compress first and quickly, while the least open and smallest defects need to be closed at higher stresses. The degree of compaction of rock changes from fast to slow. Therefore, the shape of the dissipation energy curve changes from concave to convex at an obvious inflection point (point P in Fig. 15).

Stage III: linear elasticity—absolute energy hardening. Under increasing axial compression, compacted rock undergoes only elastic deformation, and almost all the external work is converted into elastic energy and stored in the rock without energy dissipation, causing the energy ratio to increase continuously. In this stage, the released internal energy quickly accumulates to act as the energy source that drives the beginning of the next stage.

Stage IV: crack propagation—stable damage dissipation. New cracks in rock are generated by concentrated stress. Rock damage is aggravated gradually due to the continuous growth and appearance of cracks. In this stage of damage, due to the relatively small crack density and insignificant attenuation of axial stiffness associated with the axial extension of cracks, elastic energy can still accumulate rapidly. From an energy-driven point of view, although the ability of rock to store internal energy becomes attenuated in this stage,

a high energy storage rate is still maintained to provide sufficient energy for driving the initiation of isolated cracks. As the cracks propagate independently, energy is continuously and steadily dissipated in the forms of surface energy of new cracks and plastic potential energy in the vicinity of crack tips. Consequently, the energy ratio curve slowly slopes upward.

Stage V: crack propagation—accelerated damage dissipation. Independent cracks begin to influence one other and coalesce, resulting in the accelerated propagation of cracks. In this stage, appreciable rock damage is accompanied by a sharp increase in crack density. The phenomena of local microscopic slip and friction inevitably occur due to the appearance of some secondary shear cracks inclined toward the axial stress. In addition, the intensified damage and remarkable attenuation of axial stiffness lead to a lessened ability to store internal energy and a decrease in the elastic energy accumulation rate. Instead, considerable external work is converted into energy that is dissipated for the generation of crack surfaces and plastic deformation, especially for overcoming crack friction. From an energy-driven point of view, a high energy storage rate is unnecessary to supply continuous and much energy to induce new cracks because unstable cracks easily propagate and coalesce in this stage. A downward slope of the energy ratio curve occurs in response to the decrease in the elastic energy accumulation rate and intense energy dissipation.

The dissipation energy curve corresponds to the various stages of deformation and failure of rock. Energy dissipation, recognized as the essential attribute of deformation and failure of rock, presents the continuous development of internal defects in rock and the gradual loss of strength. Since damage and strength loss are inseparable from energy dissipation, normalized dissipation energy is often used as an energy damage index to measure the degree of rock damage. The curves of energy damage for the tested schist specimens (shown in Fig. 16) reveal a close dependence of damage development of schistose rock on schistosity orientation. At the points of crack initiation and crack damage, the degree of damage of schist is obviously higher at $\alpha = 30°$ than at $\alpha = 0°$ and 90°. In addition, as shown in Fig. 16, after crack initiation, the normalized dissipation energy curve of schist rises with a steeper slope at $\alpha = 0°$ and 30° relative to that at $\alpha = 90°$. This suggests that once new cracks appear, the damage develops more rapidly in specimens with $\alpha = 0°$ and 30° (and they undergo a shorter history from crack initiation to formation of fracture planes) than specimens with $\alpha = 90°$. In contrast, the damage in specimens with $\alpha = 90°$ has more obvious characteristics of gradual development, similar to isotropic rocks.
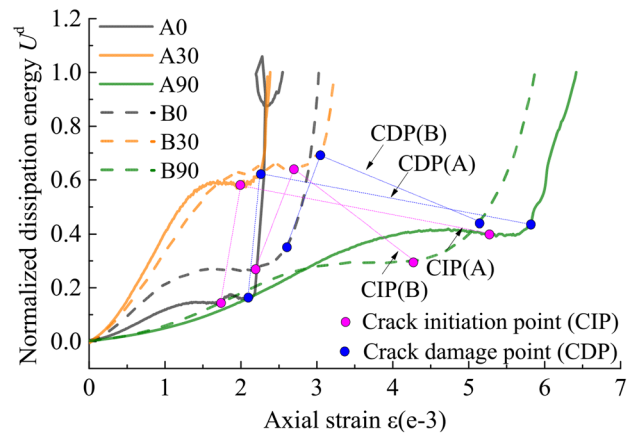

Fig. 16 Energy damage evolution of schist specimens

Previous studies have indicated that the peak strength measured by laboratory tests is a short-term loading strength (Schmidtke and Lajtai 1985; Martin and Chandler 1994). As the loading rate decreases, the peak strength gradually approaches the crack damage strength (Martin and Chandler 1994). Therefore, it is believed that the crack damage strength can be used as a reliable index for the evaluation of the long-term stability of rock masses in practical geotechnical engineering projects. However, it is worth noting that for schistose rock subjected to compression at an angle of approximately 30°, there is a rapid development of new cracks and considerable degree of damage at the point of crack damage. In this case, taking the crack damage strength as a long-term index produces a low safety margin of engineering evaluation.

Conclusions

In this study, uniaxial compression testing was carried out on cylindrical specimens of quartz mica schist with representative schistose angles. The commonly used volume strain method cannot effectively determine the crack damage strength of rock with weak planes in a specific loading direction. By virtue of the energy evolution curves (dissipation energy and energy ratio curves), the critical characteristic strengths (CCSs), i.e., the initiation, closure, and damage strength of cracks in schist specimens subjected to uniaxial continuous loading, can be accurately obtained. Based on the characteristics of crack evolution and shapes of energy curves, the deformation and failure of compressed rocks can be divided into five stages: instantaneous loading—initial stress distribution (I), compaction—initial energy dissipation (II), linear elasticity—absolute energy hardening (III), crack propagation—stable damage dissipation (IV), and crack propagation—accelerated damage dissipation (V).

Before the peak value of axial stress, each dissipation energy–axial strain curve always has the shape of an ascending ladder for all schist specimens. The dissipation energy curve shows different forms of rising in the stages II, IV, and V. Stage II exhibits an *S*-shape, with the slope first increasing and then decreasing due to gradual closure of original cracks. In stages IV and V, the development of new cracks in rock accelerates the upward slope of the energy dissipation curve. For stage III, since the rock has been compacted into an approximately elastic material, the external work is converted into elastic energy to be stored, leading to the appearance of a platform in the energy dissipation curve. Once rock enters stage V, accelerated crack propagation aggravates rock damage characterized by a sharp increase in dissipation energy, resulting in a decreasing energy ratio (ratio of elastic energy to total energy), which increased in stages II, III and IV.

Micro tests reveal that mica minerals in the tested schist are prone to cluster into weak layers that combine with hard layers composed of granular minerals to form an interbedded quasi-microstructure. Owing to this typical microstructure, the characteristics of macroscale fractures and microscale crack initiation and propagation in schist change with the loading direction angle α (schistose angle between the loading direction and schistosity plane). At both $\alpha = 0°$ and $30°$, cracks tend to develop along weak planes. However, at $\alpha = 0°$, new cracks are initiated by the concentration of tensile stress, which is mainly distributed at the interfaces between weak and hard layers and at the tips of existing oriented microcracks. The cracks in different layer levels gradually connect to form multiple fracture planes, leading to splitting failure on a macroscopic scale, mainly along the schistosity planes. At $\alpha = 30°$, the concentration of tensile stress is caused by sliding of cleavage planes of mica and microcrack surfaces. Then, a few intergranular cracks propagate rapidly and form macroscale sliding failure guided by schistosity planes. At $\alpha = 90°$, stress tends to concentrate at the ends of randomly distributed defects and interfaces between soft flaky and hard granular minerals. Tensile cracks initiate in the granular mineral zones or layers. Large numbers of complex cracks form macroscopic fracture planes oblique to schistosity planes.

The dependence of the CCS and energy of schist on the loading direction is closely related to its anisotropy in crack initiation and propagation. Data analysis reveals that at $\alpha = 0°$ and $30°$, schist undergoes more rapid damage development than at $\alpha = 90°$ after new cracks arise. The minimum crack initiation stress, highest level of crack initiation stress, and minimum energy dissipated for crack development correspond to $\alpha = 30°$. In contrast, the specimen with $\alpha = 90°$ has the lowest level of crack damage stress and larger values of elastic and dissipation energy, which shows relatively obvious gradual crack evolution under compression.

For schistose rocks with the same mineral composition, the characteristics of crack propagation closely depend on microscale factors. At $\alpha = 0°$ and $30°$, cracks propagate along the extension direction of weak layers, resulting in relatively flat fracture surfaces in the case of highly aggregated flaky minerals, mica clusters with good continuity in the same layer level, and short rock bridges composed of hard granular minerals. In the opposite case, the connected cracks deviate from the extension direction of weak layers, leading to relatively rough fracture surfaces. As a result, the mechanical behavior of schist invariably changes with its microscale factors. Especially at $\alpha = 30°$, there is a more sensitive response of the CCS and energy of schistose rocks to microscale factors. In comparison, at $\alpha = 90°$, microscale factors have less influence on mechanical behavior due to the comprehensive influence of the proportions of minerals with diverse properties and the barrier mechanism of mica clusters on crack propagation.

References

Bańka P, Chmiela A, Menéndez Fernández M et al (2017) Predicting changes in induced seismicity on the basis of estimated rock mass energy states. Int J Rock Mech Min Sci 95:79–86

Bieniawski ZT (1967) Mechanism of brittle fracture of rock, Parts I, II and III. Int J Rock Mech Min Sci Geomech Abstr 4(4):395–430

Bieniawski ZT (1974) Estimating the strength of rock materials. J South Afr Inst Min Metall 74(8):312–320

Bobet A, Einstein HH (1998) Fracture coalescence in rock-type material under uniaxial and biaxial compressions. Int J Rock Mech Min Sci 35(7):863–888

Cai MF, Wang JA, Wang SH (2001) Analysis on energy distribution and prediction of rock burst during deep mining excavation in Linglong Gold Mine. Chin J Rock Mech Eng 20(1):38–42

Chang C, Haimson B (2000) True triaxial strength and deformability of the German Continental Deep Drilling Program (KTB) deep hole amphibolite. J Geophys Res Solid Earth 105(B8):18999–19013

Chen GQ, Wu JC, Jiang WZ, Li SJ, Qiao ZB, Yang WB (2020) An evaluation method of rock brittleness based on the whole process of elastic energy evolution. Chin J Rock Mech Eng 39(5):901–911

Chen ZQ, He C, Wu D, Gan LW, Xu GW, Yang WB (2018) Mechanical properties and energy damage evolution mechanism of deep-buried carbonaceous phyllite. Rock Soil Mech 39(2):445–456

Cho JW, Kim H, Jeon S, Min KB (2012) Deformation and strength anisotropy of Asan gneiss, Boryeong shale, and Yeoncheon schist. Int J Rock Mech Min Sci 50:158–169

Diederichs MS, Kaiser PK, Eberhardt E (2004) Damage initiation and propagation in hard rock during tunnelling and the influence of near-face stress rotation. Int J Rock Mech Min Sci 41(5):785–812

Donath FA (1964) Strength variation and deformational behavior in anisotropic rock. In: W.R. Judd (Ed) State of Stress in the Earth's Crust. Elsevier, New York, 281–297

Duveau G, Shao JF, Henry JP (1998) Assessment of some failure criteria for strongly anisotropic geomaterials. Mech Cohes-frict Mat 3(1):1–26

Eberhardt E, Stead D, Stimpson B, Read RS (1998) Identifying crack initiation and propagation thresholds in brittle rock. Can Geotech J 35(2):222–233

Eberhardt E, Stead D, Stimpson B (1999) Quantifying progressive pre-peak brittle fracture damage in rock during uniaxial compression. Int J Rock Mech Min Sci 36(3):361–380

Federico A, Stefano Z, Giovanni B (2014) Fabric controls on the brittle failure of folded gneiss and schist. Tectonophysics 637:150–162

Gholami R, Rasouli V (2014) Mechanical and elastic properties of transversely isotropic slate. Rock Mech Rock Eng 47(5):1763–1773

Gottschalk RR, Kronenberg AK, Russell JE, Handin J (1990) Mechanical anisotropy of gneiss: failure criterion and textural sources of directional behavior. J Geophys Res Solid Earth 95(B13):21613–21634

Griffith AA (1921) The phenomena of rupture and flow in solids. Philos T Roy Soc A 221:163–198

Hoek E (1964) Fracture of anisotropic rock. J S Afr Inst Min Metall 64(10):501–523

Hoek E, Bieniawski ZT (1965) Brittle fracture propagation in rock under compression. Int J Fract 1(3):137–155

Khanlari G, Rafiei B, Abdilor Y (2015) An experimental investigation of the Brazilian tensile strength and failure patterns of Laminated Sandstones. Rock Mech Rock Eng 48(2):843–852

Kidybinski A (1981) Bursting liability indices of coal. Int J Rock Mech Min Sci Geomech Abstr 18(4):295–304

Kim H, Cho JW, Song I, Min KB (2012) Anisotropy of elastic moduli, P-wave velocities, and thermal conductivities of Asan Gneiss, Boryeong Shale, and Yeoncheon Schist in Korea. Eng Geol 147–148(5):68–77

Li ZG (2017) Generating relations between geological disaster and engineering properties of metamorphic rocks in Duhe River Basin, PhD Thesis, China University of Geosciences

Liu ZX, Wang W, Luo JA, Miao GH (2020) Method of energy evolution of rock under uniaxial compression test. J China Coal Soc 45(9):3131–3139

Martin CD, Chandler NA (1994) The progressive fracture of Lac du Bonnet granite. Int J Rock Mech Min Sci Geomech Abstr 31(6):643–659

Matsushima S (1960) On the deformation and fracture of granite under high confining pressure. Bull-Disast Prev Res Inst, Kyoto Univ 36:11–20

Mclamore R, Gray KE (1967) The mechanical behavior of anisotropic sedimentary rocks. J Eng Ind 89(1):62–73

Nasseri M, Rao KS, Ramamurthy T (2003) Anisotropic strength and deformational behavior of Himalayan schists. Int J Rock Mech Min Sci 40(1):3–23

Niandou H, Shao JF, Henry JP, Fourmaintraux D (1997) Laboratory investigation of the mechanical behaviour of Tournemire Shale. Int J Rock Mech Min Sci 34(1):3–16

Ohtsu M, Isoda T, Tomoda Y (2007) Acoustic emission techniques standardized for concrete structures. J Acoust Emis 25:21–32

Paulding BW (1965) Techniques used in studying the fracture mechanics of rock. Am Soc Testing & Matls Spec Tech Publ 402:73–86. https://doi.org/10.1520/STP45137S

Ramamurthy T, Rao GV, Singh J (1993) Engineering behaviour of phyllites. Eng Geol 33(3):209–225

Rao KS, Rao GV, Ramamurthy T (1986) A strength criterion for anisotropic rocks. Indian Geotech J 16: 317-333

Rawling GC, Baud P, Tengfong W (2002) Dilatancy, brittle strength, and anisotropy of foliated rocks: experimental deformation and micromechanical modeling. J Geophys Res 107(B10):2234–2247

Sagong M, Bobet A (2002) Coalescence of multiple flaws in a rock-model material in uniaxial compression. Int J Rock Mech Min Sci 39(2):229–241

Saroglou H, Tsiambaos G (2008) A modified Hoek-Brown failure criterion for anisotropic intact rock. Int J Rock Mech Min Sci 45(2):223–234

Schmidtke RH, Lajtai EZ (1985) The long-term strength of Lac du Bonnet granite. Int J Rock Mech Min Sci Geomech Abstr 22(6):461–465

Shea WT, Kronenberg AK (1993) Strength and anisotropy of foliated rocks with varied mica contents. J Struct Geol 15(9–10):1097–1121

Tapponier P, Brace WF (1976) Development of stress induced micro-cracks in Westerly granite. Int J Rock Mech Min Sci Geomech Abstracts 13:103–112

Tien YM, Kuo MC, Juang CH (2006) An experimental investigation of the failure mechanism of simulated transversely isotropic rocks. Int J Rock Mech Min Sci 43(8):1163–1181

Walsh JB, Brace WF (1964) A fracture criterion for brittle anisotropic rock. J Geophys Res 69(16):3449–3456

Wang CL, Hou XL, Li HT, Zhang SJ, Tao ZG (2019) Experimental investigation on dynamic evolution characteristics of micro-cracks for sandstone samples under uniaxial compression. Bull-Disast Prev Res Inst, Kyoto Univ 41(11):2120–2125

Wang ZQ, Yan EC, Liu YX, Wang ZJ (2014) Anisotropic properties of deformation parameters and its mechanism of Wudang group schist. Rock Soil Mech 35(5):1317–1322

Xie HP, Ju Y, Li LY (2005) Criteria for strength and structural failure of rocks based on energy dissipation and energy release principles. Chin J Rock Mech Eng 24(17):3003–3010

Xu JB (2018) Study on the creep characteristics of the surrounding rock of Wudang schist tunnel and its influence on the lining cracking, PhD Thesis, China University of Geosciences

Yang JM, Qiao L, Li Y, Li QW, Li M (2019) Effect of bedding dip on energy evolution and rockburst tendency of loaded phyllite. Chin J Eng 41(10):1258–1265

Yin XM (2017) The anisotropy of Wudang group schist and its application in tunnel support, PhD Thesis, China University of Geosciences

Yin XM, Yan EC, Wang LN, Liu LC, Feng B, Wang PZ (2020) Anisotropy of quartz mica schist based on quantitative extraction of fabric information. Bull Eng Geol Env 79(5):2439–2456

Zhang J, Ai C, Li YW, Zeng J, Qiu DZ (2017) Brittleness evaluation index based on energy variation in the whole process of rock failure. Chin J Rock Mech Eng 36(6):1326–1340

Zhou H, Meng FZ, Zhang CQ, Yang FJ, Lu JJ (2015) Characteristics and mechanism of occurrence of stress thresholds and corresponding strain for hard rock. Chin J Rock Mech Eng 34(8):1513–1521